A MULTI-PROXY REDUCED DIMENSION RECONSTRUCTION OF LGM EQUATORIAL PACIFIC SEA SURFACE TEMPERATURES

by

EMILY ELIZABETH ROEDER

B.S., United States Air Force Academy, 2020

A thesis submitted to the

Faculty of the Graduate School of the

University of Colorado in partial fulfillment

of the requirements for the degree of

Master of Science

Department of Geological Sciences

2021

Committee Members:

Julio Sepúlveda

Thomas Marchitto

Peter Molnar

ABSTRACT

Roeder, Emily Elizabeth (M.S., Geology [Department of Geological Sciences])

A Multi-Proxy Reduced Dimension Reconstruction of LGM Equatorial Pacific Sea Surface Temperatures

Thesis directed by Professor Thomas M. Marchitto

There is still a longstanding debate as to how the El Niño-Southern Oscillation (ENSO) will change as a result of global warming. Studying the tropical climate during past periods with different climatic boundary conditions can be beneficial in understanding how our climate will respond to anthropogenic forcings and may help us better understand future ENSO conditions. The Last Glacial Maximum (LGM, 19-23 ka) has been widely studied and many of its boundary conditions (e.g., atmospheric CO_2, global ice volume) have been well constrained. Yet there is no consensus on the mean state of LGM tropical Pacific sea surface temperatures (SSTs), despite its importance for the ENSO phenomenon. Utilizing a reduced-dimension methodology approach based on the work of *Mann et al.* (1998) and adapted in *Gill et al.* (2016) and *Wycech et al.* (2020), we reconstruct spatial and temporal snapshots of equatorial Pacific LGM SST anomalies using a compilation of previously published Mg/Ca and $U^{k'}37$ data from the LGM and Late Holocene. We find a full field mean cooling of 2.26°C ± 0.39°C, with the least amount of cooling in the central Equatorial Pacific. Our results suggest that there may have been a central Pacific El Niño-like mean state during the LGM.

PLAIN LANGUAGE SUMMARY

The Last Glacial Maximum (LGM, 19-23 ka) was the most recent time in Earth history when ice sheets were at their maximum extent. There are numerous paleoclimate reconstructions of the LGM, yet there is no consensus on the tropical Pacific climatic conditions during this period. We apply a statistical method approach using previously published data to infer sea surface temperatures and anomalies of the equatorial Pacific Ocean during the LGM. We find a full field mean cooling of 2.26°C ± 0.39°C, with the least amount of cooling in the central Equatorial Pacific. Our results suggest that there may have been a central Pacific El Niño-like mean state during the LGM.

CONTENTS

TABLES

Table

FIGURES

Figure

CHAPTER I

INTRODUCTION

The late Pleistocene ice ages were globally the coldest intervals of the entire Cenozoic (Zachos et al., 2001). The Last Glacial Maximum (LGM, 19-23 ka) was the most recent of these, and the best studied, due in part to the accessibility of its paleoclimate records. Many of the boundary conditions during this period (e.g., atmospheric CO_2, global ice volume) have been well constrained (Solomon et al., 2007), and hence the LGM provides an outstanding opportunity to study the response of Earth's climate to extreme radiative forcings. Analysis of a specific region during this period could provide an understanding of how our climate will respond to increasing levels of CO_2 in the environment.

There were two major projects that aimed to produce a map of climate conditions during the LGM. The first was CLIMAP—Climate: Long range Investigation, Mapping, and Prediction—which produced a reconstruction of 1-2°C SST cooling over large swaths of the tropical ocean (CLIMAP Project Members, 1976). The follow-up to CLIMAP was MARGO—Multiproxy Approach for the Reconstruction of the Glacial Ocean surface. MARGO estimated an average global tropical ocean cooling (between 15°S and 15°N) of 1.7 ±1°C and found the average mean annual cooling in the 15°S –15°N tropical band was less pronounced in the Pacific (−1.2±1.1°C) than in the Indian (−1.4±0.7°C) and Atlantic oceans (−2.9±1.3°C) during the LGM (2009). Specifically in the central equatorial Pacific, both MARGO and CLIMAP found little to no SST change (CLIMAP Project Members, 1976; MARGO Project Members, 2009).

The LGM equatorial Pacific region has been considered an ideal target for estimating the climate's response to radiative forcing. This is often measured by equilibrium climate sensitivity (ECS) (Hargreaves et al., 2012), which is defined as the global mean surface air temperature response to a doubling of atmospheric CO_2 (Charney et al., 1979). Currently, the magnitude and spatial pattern of the equatorial Pacific SST changes remain uncertain (Monteagudo et al., 2021). CLIMAP and MARGO have been controversial and disagree with climate models, which suggest a 2-2.5°C cooling in the central region (Brady et al., 2013; DiNezio et al., 2011; Otto-Bliesner et al., 2009).

The equatorial Pacific region also features interannual sea surface temperature (SST) and wind anomalies due to the El Niño Southern Oscillation (ENSO) phenomenon, which is a coupled ocean-atmosphere fluctuation in SSTs and air pressure across the equatorial Pacific. ENSO is the leading contributor to interannual variability across the globe (Rasmusson and Carpenter, 1982) and directly or indirectly affects many people globally. Redistributions of heat and moisture fluxes globally can cause disruptions economically and socially. For instance, typically wet areas like coastal Australia become drought ridden in an El Niño as the coastal warm waters become cold. Model simulations and proxy reconstructions of ENSO in various past climates, such as the LGM, can be beneficial in understanding and predicting future ENSO responses but the results remain elusive.

The gold standard for reconstructing past ENSO variability is coral fossils. However, since LGM sea levels were about 120 m lower than modern, drowned corals are hard to access. Paleo reconstructions use other methods, including but not limited to isotopic analysis ($\delta^{18}O$) (Koutavas and Lynch-Stieglitz, 2003; Leduc et al., 2009; Martinez et al., 2003) and assemblage data (Grelaud et al., 2009). Some paleo reconstructions based on individual foraminifera analysis

(IFA) find reduced ENSO variability (Ford et al., 2015; Leduc et al., 2009), while others find an increase in ENSO variability (Koutavas and Joanides, 2012; Sadekov et al., 2013). GCMs, too, tend to disagree on ENSO variability.

ENSO may be related to the mean state of the tropical Pacific and currently, the magnitude and spatial pattern of the equatorial Pacific SST changes remain uncertain (Monteagudo et al., 2021). A recent study introduced the first estimates of central equatorial Pacific LGM SSTs from a planktic species of foraminifera (forams) *Globigerinoides ruber* near the Line Islands (Monteagudo et al., 2021). These cores show a central equatorial Pacific cooling of about 2.0°C during the LGM, which is in contrast with previous global compilations (MARGO and CLIMAP), but in agreement with previous models (Brady et al., 2013; Dinezio et al., 2011) and proxy records from the Pacific (Benway et al., 2006; Bolliet et al., 2011; Dang et al., 2020; Hertzberg et al., 2016; Koutavas and Joanides, 2012; Leduc et al., 2007; Xu et al., 2010).

We utilize a reduced-dimension methodology based on the work of Mann et al. (1998) and adapted in Gill et al. (2016) and Wycech et al. (2020) to reconstruct spatial and temporal snapshots of equatorial Pacific LGM sea surface temperature (SST) anomalies from previously published Mg/Ca and $U^{k'}37$ SST records. This study was motivated, in part, by the availability of geochemical paleotemperature data from the central equatorial Pacific (Monteagudo et al., 2021). Having data from all regions of the equatorial Pacific allows for a more robust and reliable reconstruction of LGM conditions.

DATA

Our reduced-dimension approach uses the relationship between the full field contemporary SSTs (i.e., at every grid cell within our spatial domain) and the limited field Mg/Ca (Figure 1a) and $U^{k'}37$ (Figure 1b) core locations to reconstruct a full field SST map of the LGM equatorial Pacific.

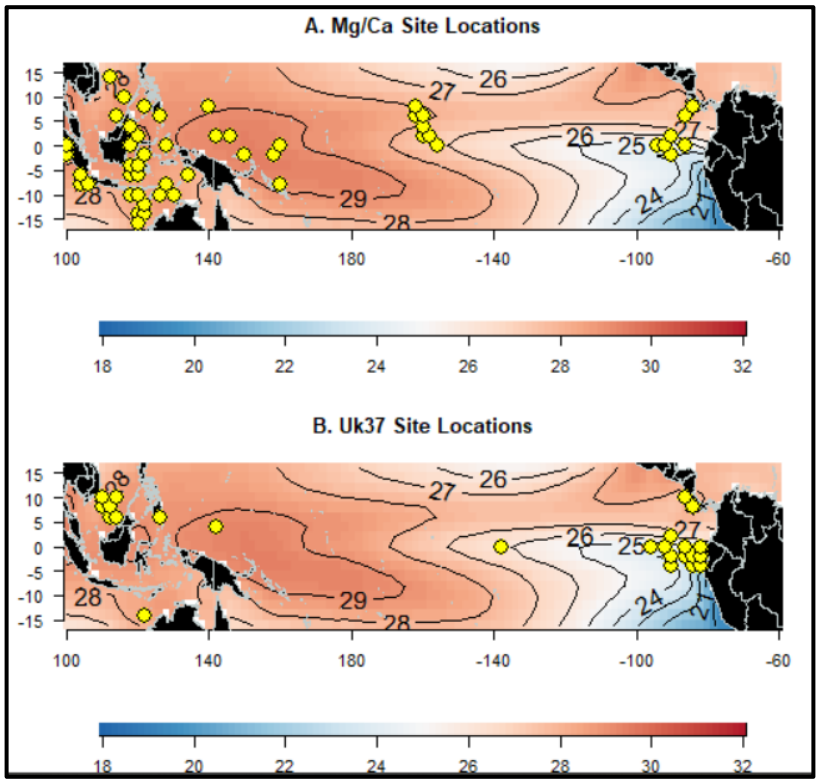

Figure 1. (a) Limited field Mg/Ca and (b) $U^{K'}_{37}$ site locations, plotted over modern mean annual SSTs from ERSST (Smith et al., 2008).

Contemporary Data

Contemporary SST data is sourced from the NOAA National Climatic Data Center (NCDC) Extended Reconstruction Sea Surface Temperature (ERSST) version 3b data set (Smith et al., 2008). The contemporary monthly SSTs, gridded 2° × 2° and averaged from 1854 to 2018, represent the equatorial region from 16°S to 16°N and 100°E to 60°W. We calculate monthly

anomalies using the 1981-2010 climatology and average from May to April to produce annual averages. This time frame best captures the annual ENSO cycle in the equatorial Pacific as it is strongest during the boreal winter.

Paleo-SST data

Our Paleo-SST data is compiled from previously published data from two widely used marine geochemical proxies: Magnesium-calcium paleothermometry (Mg/Ca) and the $U^{K'}_{37}$ index. Mg/Ca is a common proxy for estimating SSTs that exploits the ratios of magnesium to calcium in planktonic foraminifera (foram) calcite tests. From experiments on both synthetic calcite growth and experiments using living organisms, it has been determined that, at higher temperatures, more magnesium is incorporated into the calcite tests (Lowenstein and Hönisch, 2012). Thus, we can measure the Mg/Ca ratio in the test to determine the temperature of the water at the time of calcification. The $U^{K'}_{37}$ index, another successful proxy-indicator of SST, is derived from the relative abundance of alkenones (unsaturated ketones produced by phytoplanktonic algae) found in marine sediments (Rosell et al., 1994). More specifically, the $U^{K'}_{37}$ unsaturation index is defined by the ratio between the diunsaturated ($C_{37:2}$) alkenones to the sum of diunsaturated and triunsaturated ($C_{37:3}$) alkenones, $U^{K'}_{37} = C_{37:2}/(C_{37:2} + C_{37:3})$ (Brassell et al., 1986; Marlowe et al., 1984; Prahl and Wakeham, 1987; Volkman et al., 1980). Previous constructions using our methodology included other proxies such as TEX_{86}, and foraminifer assemblages (Wycech et al., 2020) and ice core/ice melt proxies, corals, tree rings, and $\delta^{18}O$ (Mann et al., 2008). Though we only used two proxies—Mg/Ca and $U^{k'}37$—these supplied a large number of site locations and we could therefore perform a thorough reconstruction. Since each proxy type has its own structural biases, the use of multiple proxies

may help to offset those biases when used together. With both Mg/Ca and $U^{K'}_{37}$ data, we can create a more robust estimate of LGM SSTs and full field anomalies.

Previously published late Holocene (LH) (4-0 ka) and LGM (23-19 ka) Mg/Ca and $U^{K'}_{37}$ data were obtained from compilations in two recent studies: Monteagudo et al. (2021) and Tierney et al. (2020). Though the two studies presented data from multiple oceans and several proxies, we only used Mg/Ca and $U^{K'}_{37}$ data between 16°N-16°S and 100°E-60°W, excluding sites in the Caribbean. The multi-proxy data (See *Appendix* Table A1) features 94 cores located between 15.31°S-14.80°N and 99.91°E-81.31°W and includes 67 Mg/Ca and 27 $U^{K'}_{37}$ core sites.

Monteagudo Data

The Monteagudo et al. (2021) compiled data is solely Mg/Ca from the surface dwelling planktic foraminifer *G. ruber*. This dataset contributes 65 of the 94 total sites and comprises most of the central equatorial Pacific data used in this study. The only sites excluded from the Monteagudo dataset were those that fell outside the longitudinal boundaries; no sites were outside the latitudinal boundaries since their study also focused on the equatorial region. The Mg/Ca data was originally calibrated using the Dekens et al. (2002) equation for *G. ruber* using modern seafloor $\Delta[CO_3^{2-}]$ as a dissolution correction. This equation with the dissolution correction was appropriate since partial dissolution is prevalent in the equatorial Pacific (e.g. Mekik et al., 2007; Rongstad et al., 2017; Wycech et al., 2018). Additionally, Monteagudo et al. (2021) adjusted their Mg/Ca temperature estimates by 0.6°C, since that was the mean offset found between the modern climatology and the LH Mg/Ca SST values. This prevents an overestimation of the magnitude of LGM cooling, and we kept this 0.6°C throughout our data set as well. For the Monteagudo et al. (2021) sites that did not have LH data, we used the contemporary ERSST data set as estimates. The contemporary values from this data set were not

significantly different from the Monthly Isopycnal & Mixed-layer Ocean Climatology (MIMOC) used in the Monteagudo study.

Tierney Data

The Tierney et al. (2020) data makes up the other 29 of the 94 sites and includes both Mg/Ca (2 sites) and $U^{K'}_{37}$ (27 sites) SSTs. Tierney et al. (2020) Mg/Ca was only included if the core was missing from the Monteagudo et al. (2021) compilation. Although the original Tierney et al. (2020) dataset included two *G. sacculifer* Mg/Ca within our spatial domain, we opted to exclude them because *G. sacculifer* calcifies slightly deeper than *G. ruber* on average (Rippert et al., 2016), including an additional calcite crust formed during gametogenesis (Bé, 1980; Bé et al., 1983). This dataset included several other proxies that we did not use, including TEX_{86} and $\delta^{18}O$. The fraction of TEX_{86} to the total data in the Tierney et al. (2020) dataset was small, and it has been suggested that there are confounding effects of this proxy (Qin et al., 2015) that could have made our overall reconstruction less robust. The $\delta^{18}O$ of planktonic foraminifera can be used as a proxy for SST used in conjunction with other proxies. However, the $\delta^{18}O$ of their shells primarily reflects changes in ice volume and freshwater input to the ocean (Ravelo and Hillaire-Marcel, 2007), so we opted not to use this proxy either.

Tierney et al. (2020) converted Mg/Ca to temperature using a multivariate Bayesian calibration (Tierney et al., 2019). To maintain consistency with the Monteagudo et al. (2021) datasets, we recalibrated the Tierney Mg/Ca sites using the Dekens et al. (2002) dissolution correction equation with +0.6°C adjustment. To obtain proper estimates of the $\Delta[CO_3^{2-}]$ for the Tierney sites, we calculated the seafloor $\Delta[CO_3^{2-}]$ values using total alkalinity and total dissolved inorganic carbon from the nearest World Ocean Circulation Experiment (WOCE) transects and the carbonate system calculator CO2Sys (version 2.1 for Excel) with default

dissociation constants (Lewis and Wallace, 1998). The $U^{K'}_{37}$ Bayesian calibration (Tierney and Tingley, 2018) used by Tierney et al. (2020) was plotted against the Dekens et al. (2002) values (see Figure A1). The two groups could not be proven to be significantly different (see Text A1). For those sites without LH data (both Mg/Ca and $U^{K'}_{37}$), the contemporary ERSST values were again used.

As seen in Table A1, the full range of Mg/Ca values is 2.46—5.35 mmol/mol (LH) and 1.97—4.27 mmol/mol (LGM). The range of UK′37 values is 0.794—0.972 (LH) and 0.728—0.974 (LGM). Cores that fell into the same 2° × 2° grid cell were averaged, and the final dataset used for the multiproxy analysis resulted in a combined 74 site locations. In those 74 sites, the estimated range for SSTs in the equatorial Pacific ranged from 22.05-30.65°C for the LH and 20.05-29.10°C for the LGM. The average paleo SST proxy values were 27.58°C (LH) and 25.1°C (LGM). SSTs were converted to anomalies by differencing the average SST value from each of the two time slices, LGM minus LH.

METHODS

Principal Component Analysis

Our methodology of a multi-proxy, reduced-dimension analysis for reconstructing LGM SSTs is rooted in the work of Mann et al. (1998) who combined a multitude of proxies (tree rings, marine sediments, speleothems, ice cores, corals, etc.) with instrumental records to reconstruct global temperature patterns over the past six centuries. Similar methodology was adapted in Wycech et al. (2020) for the Pliocene (5.3-2.58 Ma) and in other studies for various time periods (Gill et al., 2016; Luterbacher et al., 2004; Rutherford et al., 2005). Specifically, we

use the principal component analysis (PCA) technique described in detail by Gill et al. (2016) and summarize it briefly below.

PCA is an eigenvector-based linear technique useful for orthogonalization, data compression, and filtering. Simply put, it reduces the dimensionality of a large data set into a smaller one that still contains most of the information from the larger set. It preserves as much information as possible by transforming spatiotemporal SST data into several spatial modes (the eigenvectors, or empirical orthogonal functions) and time series of those modes (the principal components). A PCA was performed on the instrumental SST data over the full field (Figure 1) and over the limited field core locations (Figures 1a and 1b). Three modes were retained for each PCA. Figure 2 shows the first three spatial modes of the PCA analyses, which together explain about 87% of the variance. Figure 2b maps the empirical orthogonal function (EOF) of the three

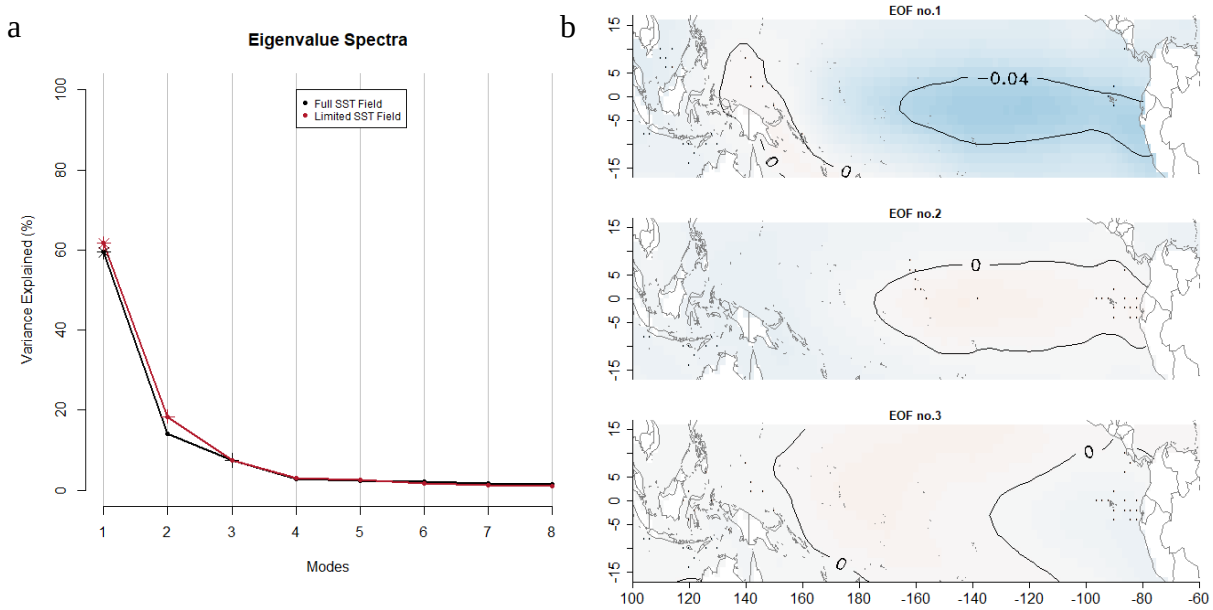

Figure 2. (a) Eigenvalue spectra for the full SST field (black) and limited SST field (red). (b) EOFs of the three leading modes of the PCA performed on the full field of instrumental SST

leading modes of the PCA performed on the instrumental full field. EOF1 likely represents variance due to ENSO, while the spatial patterns of EOF2 and EOF3 are up for interpretation.

The principal components (PC) from the full and limited fields were then linearly regressed against one another fitting three linear regression models. The PC values of the LGM SST data were calculated by multiplying SST anomalies (LGM – LH) by the limited field eigenvectors and were then used as predictors in the linear models to reconstruct the full field PCs for 21 ka. Finally, the full field paleo PCs were transformed to SST anomalies through eigenvector expansion.

To assess the accuracy of the PCA model and our ability to reconstruct ENSO-related SST patterns from the limited field core locations, we performed several tests. First, we compared actual and reconstructed Niño historical indices (Figure 3). The model fits well with

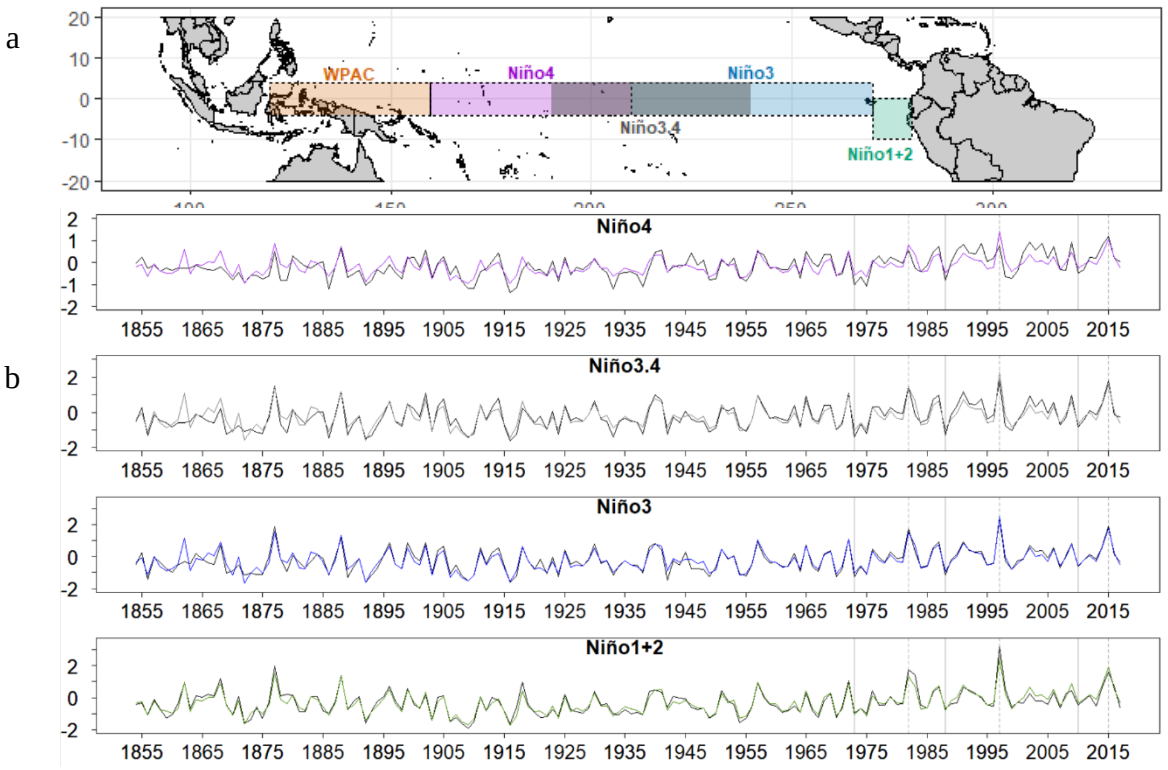

Figure 3. (a) Niño Index Regions. (b) Actual (black) and reconstructed (colors) comparison of historical Niño indices and El Niño events. Vertical dashed gray lines mark strong El Niño years and vertical solid lines mark La Niña years.

the actual indices especially in the Niño 1+2, Niño 3, and Niño 3.4 regions where we have many limited field core sites. The actual-reconstructed mismatch is greatest in the Niño 4 region where we have a sparse number of limited field sites. The Niño 3.4 index is one of the most used indices for defining El Niño and La Niña events in the Pacific Ocean, and our inclusion of the central equatorial Pacific Line Island cores from Monteagudo et al. (2021) likely increases the fidelity of that reconstruction. Even for the Niño 4 region where there are not as many sites, actual-reconstructed mismatches are in event magnitude, and the major El Niño and La Niña events are still captured.

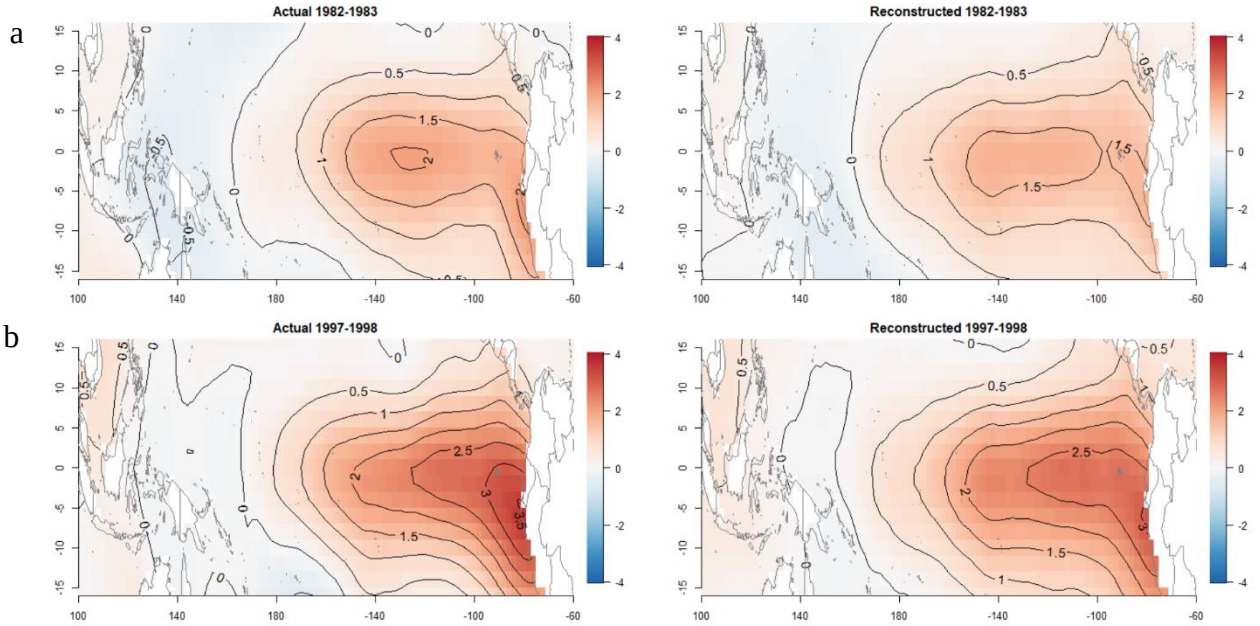

Figure 4. (a) Actual vs. Reconstructed anomalies for the 1982-1983 El Niño and (b) the 1997-1998 El Niño.

We then compared the anomaly maps (Figure 4) between the actual and reconstructed for two of the largest El Niño events since 1950—the 1982-1983 and 1997-1998 El Niños. For both reconstructed events, the spatial patterns are similar to the actual events, with a slight underestimation of maximum warming anomalies. The similarities shown in Figures 3 and 4 illustrate the robustness of our reconstruction model.

Model Assumptions

When applying a limited field approach to reconstruct LGM SSTs, we made several assumptions. We first assumed that all relationships between the limited field sites and full field were linearly related, or the PCA technique would not have worked. We also assume proxy relationships are applicable back to LGM and that their relationships to SST did not change. This is plausible considering the residence times of Ca and Mg are relatively long (10^6 and 10^7, respectively). We assume the ontogenies of the foraminifera and coccolithophores used for Mg/Ca and $U^{k'}_{37}$ were the same as today. Finally, this SST reconstruction represents the mean state of the equatorial Pacific and cannot infer interannual ENSO variability.

Because more water was harnessed in ice sheets during the LGM, sea level was much lower (~120 m) (DiNezio & Tierney, 2013). More land, including the Sunda Shelf, was exposed which resulted in weakened convection and an overall drying over the land in the western equatorial Pacific (DiNezio & Tierney, 2013). Ice sheets, and to first-order—land changes—had a large influence on the tropical climate during the LGM and should be taken into account.

RESULTS AND DISCUSSION

Multi-proxy Reconstruction

The goal of this study was to create reconstructed SST anomaly maps for the LGM. Figure 5a shows the reconstructed anomaly map with points denoting the proxy-based SST anomaly at each site. Anomalies were defined relative to the raw LH or instrumental SST for each record and contours are in increments of 0.2°C. As expected, our anomaly map shows an overall cooling in the equatorial Pacific LGM with an average full field cooling of 2.26°C ±

0.39°C. Maximum cooling is found in the eastern coastal upwelling region south of the equator. A spatial pattern of lesser cooling (i.e., relative warmth) in our LGM reconstruction trends diagonally from the northeast to the central region of the equatorial Pacific, as shown by the lighter colored areas in Figure 5a. Figure 5b shows the standard errors of the reconstructed LGM anomalies. The standard errors are small and fall between 0.1-0.3°C in the equatorial Pacific LGM. The highest error values are in the eastern equatorial Pacific where the cooling anomalies are the greatest.

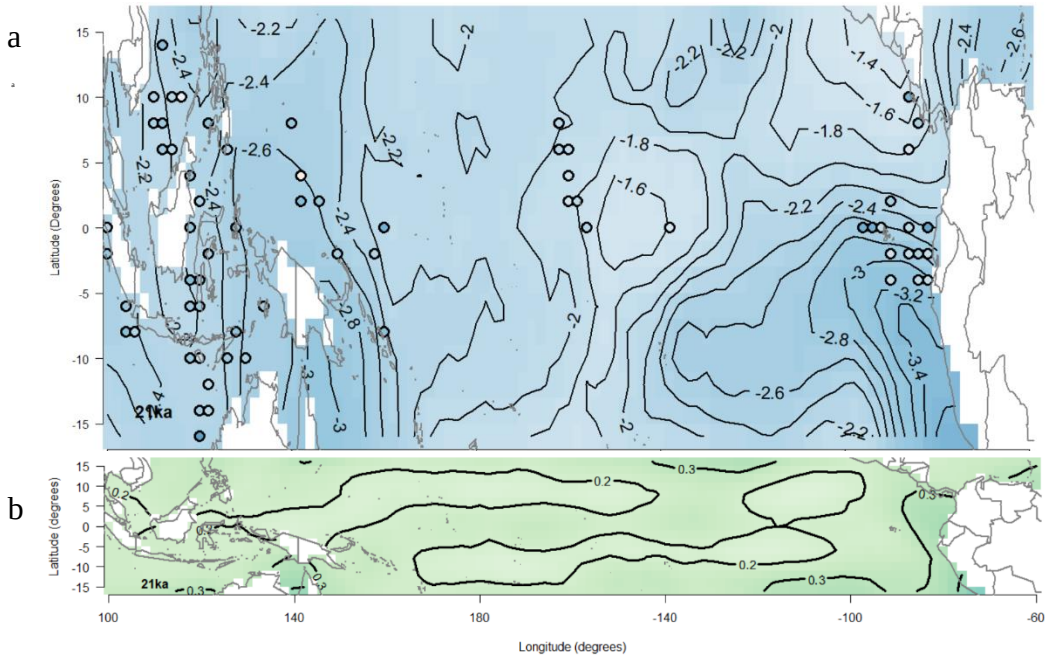

Figure 5. (a) Reconstructed LGM anomaly map with circles denoting the proxy-based SST at each site using the same color schematic. (b) Standard error map obtained from 500 ensembles of each PC.

We quantify spatial cooling by observing the average SSTs of the Niño Index regions (Figure 3a). The average cooling of each region, as well as the full field average, is shown in Table 1.

As seen in Table 1, the most cooling is found in the eastern equatorial Pacific with an average cooling of 3.09°C ± 0.30°C, with the WPAC close behind at 2.51°C ± 0.20°C. The least

Niño Index Region *(4°S to 4°N)	Longitude	Average Cooling (± standard deviation)	Anomalous Temperature Change
WPAC	120°E - 160°E	-2.51°C ± 0.20°C	-0.25°C
Niño 4	160°E - 150°W	-2.01°C ± 0.22°C	0.25°C
Niño 3.4	170°W - 120°W	-1.86°C ± 0.23°C	0.40°C
Niño 3	150°W - 90°W	-2.15°C ± 0.21°C	0.11°C
Niño 1+2	90°W - 80°W	-3.09°C ± 0.30°C	-0.83°C
Full Field	100°E - 60°W	-2.26°C ± 0.39°C	----

Table 1. Average cooling and standard deviation based on each Niño Index region. *Niño 1+2 has latitudinal boundaries of 0° to 10°S.

cooling is the central equatorial Pacific with an average cooling of 1.86°C ± 0.23°C. The Niño Index Regions are normally used to characterize the state of ENSO. For us to use them in an analogous way, we needed to remove the background cooling. The final column of Table 1 shows "Anomalous Temperature Change," which is the average cooling plus the full field average cooling value of 2.26°C. Thus, values in the last column more clearly show relative warming in the central regions and more cooling in the western and eastern regions.

Since the color schematic of both the site points and the anomaly map in Figure 5a are the same, it is easy to identify mismatches between the proxy sites and the reconstruction. The central Pacific has a good match between the two; however, we notice mismatches for certain sites in the western and eastern regions. The largest proxy-reconstruction mismatch is near 5°N, 140°E where the proxy data point shows a slight warming. To take a closer look at these proxy-reconstruction differences, we separated the proxies into two different reconstructions.

Single-proxy Reconstructions

When separating the Mg/Ca and $U^{K'}_{37}$ sites, we found similarities and differences in the anomaly maps. In both maps, the overall pattern of cooling is similar: the central Pacific is the warmest and the eastern region below the equatorial upwelling zone shows the most cooling. However, the overall magnitude of cooling is more pronounced when using only Mg/Ca sites:

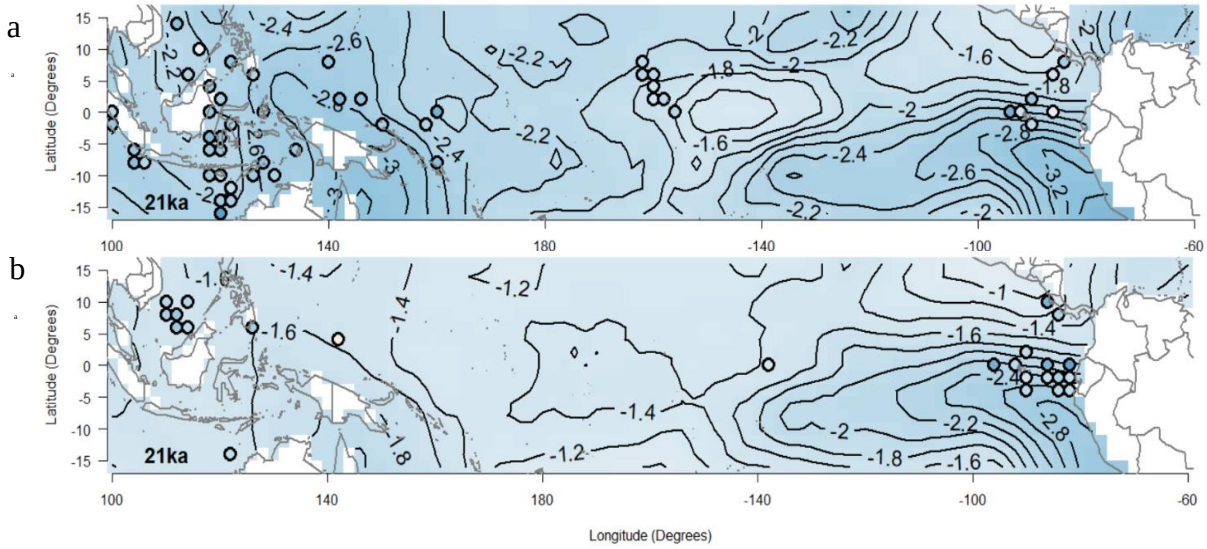

Figure 6. Reconstructed LGM anomaly maps using sites from (a) only Mg/Ca and (b) only $U^{K'}_{37}$.

the average full field anomaly using Mg/Ca sites is 2.25°C ± 0.41°C while the average anomaly using $U^{K'}_{37}$ sites is only 1.57°C ± 0.36°C. The largest cooling anomaly captured in the southeastern coastal upwelling region is 2.94°C using only $U^{K'}_{37}$ sites, compared to 3.58°C captured in the same region using Mg/Ca sites. See Table A2 for a comparison of average anomaly values and other statistics between the three reconstructions (Mg/Ca and $U^{K'}_{37}$, Mg/Ca only, $U^{K'}_{37}$ only).

It is not uncommon to see such divergent behavior between these two proxies, as each proxy likely has its own seasonal biases (e.g. Leduc et al., 2010; Schneider et al., 2010; Timmermann et al., 2014). For instance, one study found that $U^{K'}_{37}$ has a bias towards boreal winter in the western tropical Pacific, while Mg/Ca has a bias towards boreal summer in the eastern tropical Pacific (Timmerman et al., 2014). It should also be noted that the Mg/Ca sites are more numerous and more spread out over the longitudinal domain (than $U^{K'}_{37}$ sites). These two factors may play a role in the differences between the two single-proxy maps.

In some cases, separating the proxies reduces the mismatch between proxy and reconstruction, for example the cluster of modest $U^{K'}_{37}$ cooling south of the equator in the east. In other cases, the mismatch becomes worse, for example the cluster of relatively strong $U^{K'}_{37}$ cooling north of the equator in the west. Overall, the mismatches in the multiproxy anomaly map (Figure 5a) do not appear to be solely related to inter-proxy biases. For these reasons, we favor the multi-proxy anomaly map for our analysis.

Comparison to Previous Reconstructions

As previously mentioned, CLIMAP and MARGO are two of the first proxy-based reconstructions of the LGM. The results of MARGO and CLIMAP found little to no SST change in the central equatorial Pacific (CLIMAP Project Members, 1976; MARGO Project Members, 2009), which disagree with our central cooling findings of 1.85°C ± 0.23°C. It should be noted that much of the data in MARGO (and generated for CLIMAP) was assemblage data—a proxy method with many inconsistencies. Other proxy-based analyses show overall tropical cooling estimates between 2-3°C (Ballantyne et al., 2005; Crowley, 2000), which agree with our mean average cooling of 2.26°C ± 0.39°C. One study claims that the zonal gradient of the tropical Pacific during the LGM was reduced (Koutavas and Joanides, 2012), though it should be noted that no data was included from the central Equatorial Pacific in their analysis.

The most recent data-assimilated reconstruction (Tierney et al., 2020) estimates a central cooling of 3.9°C. When all proxies other than geochemical proxies are removed from the Tierney et al. (2020) analysis, the tropical SST change on average is 0.9°C smaller than in their original reconstruction (which would make their values much closer to ours). Spatially, Tierney et al. (2020) found a cooling pattern of “less cooling” to “more cooling,” moving from the western to

the eastern sides of the basin. Our reconstruction shows the least amount of cooling in the central region, which is in disagreement with their spatial pattern.

Comparison to GCM Simulations

Comparing our results to General Circulation Models (GCMs) is useful because they may offer insight into potential mechanisms; major boundary conditions, such as CO_2 and global ice volume, would result in cooling in these models. GCMs and other model simulations show varying degrees of similarity with our reconstruction. When just comparing the mean cooling values between several models (or model ensembles) and our reconstruction, the average values agree and fall between 2-3°C (Ballantyne et al., 2005; Brown et al., 2020; Otto-Bliesner et al., 2009). Some model simulations find a similar mean central equatorial Pacific cooling of ~2.0°C (Brady et al., 2013; DiNezio et al., 2011), which agrees closely with our Nino 3.4 (120°W-170°W) mean average cooling of 1.87°C ± 0.23°C. The most recent study that compared past and future simulations of ENSO in various GCMs had similar LGM mean cooling values to ours (Brown et al., 2020) and found a mean multi-model ensemble cooling of 2-3°C in the tropical Pacific (in agreement with our 2.26°C average cooling).

The diagonal spatial pattern of warmer SST anomalies in our reconstruction most closely resembled the LGM PMIP2 CCSM3 model from Otto-Bliesner (2009). Two more recent model simulations do not capture our diagonal, northeast trending, warm anomalies and show more of a La Niña-like pattern (Zhu et al., 2017) or no distinct pattern at all (Lenton et al., 2015). Compared to other past time periods, however, the LGM has much less inter-model agreement when comparing mean SST patterns and changes in amplitude of ENSO (Brown et al., 2020; Koutavas and Joanides, 2012), so it can be difficult to compare our results.

Central Pacific El Niño-Like Pattern

This study aimed to provide a multi-proxy SST reconstruction of the *mean state* of the LGM equatorial Pacific and cannot discern the *interannual variance* of ENSO, though the mean state is thought to be fundamental for the character of interannual variability (Fedorov and Philander, 2001; Guilyardi et al.,2009; Collins et al., 2010; Koutavas and Joanides, 2012). It is therefore interesting to note that our reconstruction resembles a central Pacific El Niño.

Today, El Niños have been classified as either eastern Pacific (EP) or central Pacific (CP) based on where the maximum SST anomaly occurs (Cai et al., 2018). The two are hypothesized to be fundamentally related and both start the same way. A CP El Niño dies out as it heads east, unlike an EP El Niño, which proceeds into the cold tongue (Karnauskas et al., 2013). Figure 7a shows a recent CP El Niño that occurred in 2002 (data from Smith et al., 2008), where the highest SST anomalies occurred in the central equatorial Pacific, with an axis of warmth that extends to Central America. This pattern is similar to our multi-proxy reconstruction shown in Figure 7b (note that the average full field cooling anomaly of 2.26°C was added to the reconstruction to emphasize areas of "less cooling"). Our reconstruction differs in that it shows slightly warmer temperatures off the coast of central America and colder temperatures south of the equator. This central Pacific El Niño-like state could be the result of stronger or more frequent CP El Niño events revealing themselves through the proxy data. It is possible that eastward propagation of warm Kelvin waves was inhibited by intense eastern upwelling, which is most clearly expressed south of the equator.

While the observed mean state pattern could simply be a change in SSTs without a change in interannual variability, the dynamics required to cool the eastern and western regions of the equatorial Pacific more than the central region are not obvious.

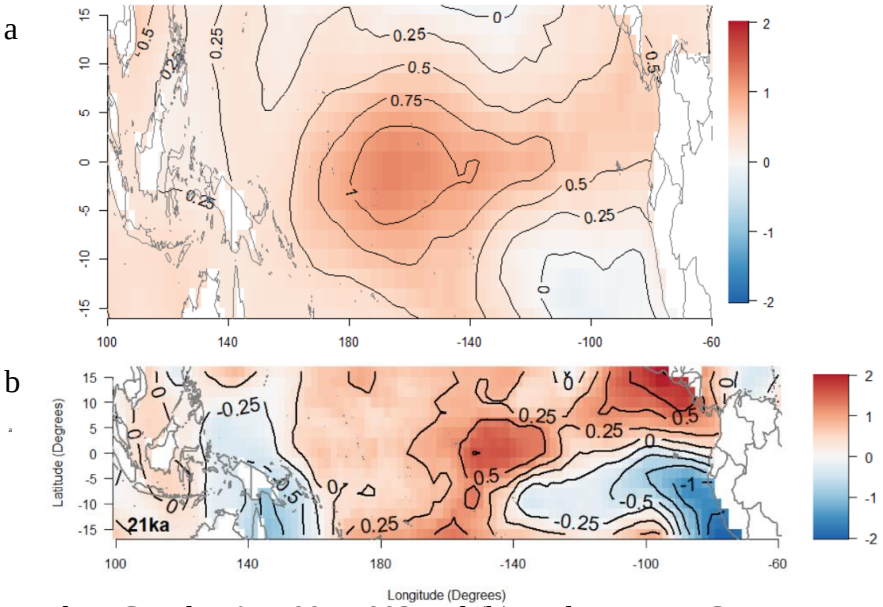

Figure 7. (a) Modern CP El Niño 2002-2003 and (b) Multi-proxy LGM reconstruction with the average cooling of 2.26°C added

There is still debate about the strength of ENSO during the LGM, with some paleo-proxy studies showing a stronger ENSO than that of the LH (Koutavas and Joanides, 2012; Sadekov et al., 2013) and some showing a weaker ENSO (Ford et al., 2015; Leduc et al., 2009). However, the existing reconstructions focus on the eastern equatorial Pacific. We suggest that reconstructions of SST variability from the central equatorial Pacific would be valuable.

Future Work

There is still a need to constrain the relationship between the LGM mean state and ENSO variability in the equatorial Pacific. The disagreement between models on LGM ENSO emphasizes the need for model development, especially for predicting ENSO changes in the modern world. Additionally, future work needs to include more data points, especially in the central Equatorial Pacific. As seen in Figure 3b, the highest mismatch between the data and our reconstructions of the Niño Indices is in the Niño 4 region, where we have the least amount of site locations.

CONCLUSION

The goal of this study was to reconstruct SST anomalies to determine the mean state of the equatorial Pacific during the LGM. We used a multi-proxy, reduced-dimension approach to reconstruct full field equatorial Pacific SST anomalies from limited core locations. The average full field cooling anomaly for the LGM equatorial Pacific region was 2.26°C ± 0.39°C, in broad agreement with other recent proxy reconstructions and GCM simulations. We found that the LGM displayed a central El Niño-like mean state, as the least amount of cooling was found in the central equatorial Pacific. Further research is still needed to constrain the relationship between equatorial Pacific mean state and ENSO variability during the LGM.

REFERENCES

Ballantyne, A. P., Lavine, M., Crowley, T. J., Liu, J., and Baker, P. B. (2005), Meta-analysis of tropical surface temperatures during the Last Glacial Maximum, *Geophys. Res. Lett.*, 32, L05712, doi:10.1029/2004GL021217.

Bé, A.W.H. (1980) Gametogenic calcification in a spinose planktonic foraminifer, Globigerinoides sacculifer (Brady). *Marine Micropaleontology*, 5. 283-310 doi:10.1016/0377-8398(80)90014-6.

Bé, A.W.H., Anderson, O.R., Faber Jr., W.W., Caron, D.A. (1983). Sequence of morphological and cytoplasmic changes during gametogenesis in the planktonic foraminifer Globigerinoides sacculifer (Brady). *Micropaleontology* 29 (3), 310–325.

Benway, H. M., Mix, A. C., Haley, B. A., & Klinkhammer, G. P. (2006). Eastern Pacific Warm Pool paleosalinity and climate variability: 0-30 kyr. *Paleoceanography*, 21, PA3008. https://doi.org/10.1029/2005PA001208.

Bolliet, T., Holbourn, A., Kuhnt, W., Laj, C., Kissel, C., Beaufort, L., et al. (2011). Mindanao dome variability over the last 160 kyr: Episodic glacial cooling of the West Pacific Warm Pool. *Paleoceanography*, 26(1), PA1208. https://doi.org/10.1029/2010PA001966.

Brady, E. C., Otto-Bliesner, B. L., Kay, J. E., & Rosenbloom, N. (2013). Sensitivity to glacial forcing in the CCSM4. *Journal of Climate*, 26(6), 1901–1925. https://doi.org/10.1175/JCLI-D-11-00416.1.

Brown, J. R., Brierley, C. M., An, S. -I., Guarino, M. -V., Stevenson, S., Williams, C. J. R., Zhang, Q., Zhao, A., Abe-Ouchi, A., Braconnot, P., Brady, E. C., Chandan, D., D'Agostino, R., Guo, C., LeGrande, A. N., Lohmann, G., Morozova, P. A., Ohgaito, R., O'ishi, R., and Zheng, W. (2020). Comparison of past and future simulations of ENSO in CMIP5/PMIP3 and CMIP6/PMIP4 models. *CLIMATE OF THE PAST*, 16 (5), pp.1777-1805. https://doi.org/10.5194/cp-16-1777-2020.

Cai, W., Wang, G., Dewitte, B., Wu, L., Santoso, A., Takahashi, K., Yang, Y., Carréric, A., & McPhaden, M. J. (2018). Increased variability of eastern Pacific El Niño under greenhouse warming. *Nature*, 564(7735), 201–206. https://doi.org/10.1038/s41586-018-0776-9.

Charney, J.G., A. Arakawa, D.J. Baker, B. Bolin, R.E. Dickinson, R.M. Goody, C.E. Leith, H.M. Stommel, and C.I. Wunsch. 1979. Carbon Dioxide and Climate: A Scientific Assessment. Report of an Ad Hoc Study Group on Carbon Dioxide and Climate, National Academy of Sciences, The National Academies Press, Washington, DC, 22 pp.

CLIMAP Project Members (1976). Modeling the ice-age climate. *Science*, 191(4232), 1138–1144. https://doi.org/10.1126/science.191.4232.1138.

Collins, M. & An, Soon-Il & Cai, Wenju & Ganachaud, Alexandre & Guilyardi, Eric & Jin, Fei-Fei & Jochum, Markus & Lengaigne, Matthieu & Power, Scott & Timmermann, Axel & Vecchi, Gabe & Wittenberg, Andrew. (2010). The impact of global warming on the tropical Pacific Ocean and El Niño. *Nature Geoscience*. 3. 391-397. 10.1038/ngeo868.

Crowley, T. J. (2000). CLIMAP SSTs re-revisited. Climate Dynamics, 16, 241–255.

Dang, H., Jian, Z., Wang, Y., Mohtadi, M., Rosenthal, Y., Ye, L., et al. (2020). Pacific warm pool subsurface heat sequestration modulated Walker circulation and ENSO activity during the Holocene. *Science Advances*, 6, 1–9.

DiNezio, P., Clement, A., Vecchi, G. A., Soden, B., Broccoli, A. J., Otto-Bliesner, B. L., & Braconnot, P. (2011). The response of the Walker circulation to last glacial maximum forcing: Implications for detection in proxies. *Paleoceanography*, 26(3), 1–21. https://doi.org/10.1029/2010PA002083.

Dinezio, Pedro & Tierney, Jessica. (2013). The effect of sea level on glacial Indo-Pacific climate. *Nature Geoscience*. 6. 485-491. 10.1038/ngeo1823.

Hargreaves, J. C., Annan, J. D., Yoshimori, M., & Abe-Ouchi, A. (2012). Can the Last Glacial Maximum constrain climate sensitivity?. *Geophysical Research Letters*, 39(24), L24702. https://doi.org/10.1029/2012GL053872.

Hertzberg, J. E., Schmidt, M. W., Bianchi, T. S., Smith, R. K., Shields, M. R., & Marcantonio, F. (2016). Comparison of eastern tropical Pacific TEX86 and Globigerinoides ruber Mg/Ca derived sea surface temperatures: Insights from the Holocene and Last Glacial Maximum. *Earth and Planetary Science Letters*, 434, 320–332. https://doi.org/10.1016/j.epsl.2015.11.0.

Fedorov, A. V., and S. G. Philander (2001), A stability analysis of tropical ocean–atmosphere interactions: Bridging measurements and theory for El Niño, *J. Clim.*, 14, 3086–3101, doi:10.1175/1520-0442(2001)014<3086:ASAOTO>2.0.CO;2.

Ford, H. L., Ravelo, A. C., and Polissar, P. J.: Reduced El Nino-Southern Oscillation during the Last Glacial Maximum, *Science*, 347, 255–258, 2015.

Gill, E. C., B. Rajagopalan, P. H. Molnar,Y. Kushnir, and T. M. Marchitto (2017), Reconstruction of Indian summer monsoon winds and precipitation over the past 10,000 years using equatorial pacific SST proxy records, *Paleoceanography*, 32, 195–216. doi:10.1002/2016PA002971.

Gill Emily C., Rajagopalan Balaji, Molnar Peter, Marchitto Thomas M. (2016). Reduced-dimension reconstruction of the equatorial Pacific SST and zonal wind fields over the past 10,000years using Mg/Ca and alkenone records. *Paleoceanography*, 31(7), 928-952.

Grelaud, M., L. Beaufort, S. Cuven, and N. Buchet (2009), Glacial to interglacial primary production and El Niño–Southern Oscillation dynamics inferred from coccolithophores of the Santa Barbara Basin, *Paleoceanography*, 24, PA1203, doi:10.1029/2007PA001578.

Guilyardi, E., A. Wittenberg, A. Fedorov, M. Collins, C. Wang, A. Capotondi, and G. J. van Oldenborgh (2009), Understanding El Niño in ocean-atmosphere general circulation models: Progress and challenges, Bull. Am. *Meteorol. Soc*., 90, 325–340, doi:10.1175/2008BAMS2387.1.

Karnauskas, K. B. (2013), Can we distinguish canonical El Niño from Modoki?, *Geophys. Res. Lett.*, 40, 5246– 5251, doi:10.1002/grl.51007.

Koutavas, A., and J. Lynch-Stieglitz (2003), Glacial-interglacial dynamics of the eastern equatorial Pacific cold tongue-Intertropical Convergence Zone system reconstructed from oxygen isotope records, *Paleoceanography*, 18(4), 1089, doi:10.1029/2003PA000894.

Koutavas, A., and Joanides, S. (2012), El Niño–Southern Oscillation extrema in the Holocene and Last Glacial Maximum, *Paleoceanography*, 27, PA4208, doi:10.1029/2012PA002378.

Leduc, G., R. Schneider, J.-H. Kim, and G. Lohmann (2010), Holocene and Eemian sea surface temperature trends as revealed by alkenone and Mg/Ca paleothermometry, *Quat. Sci. Rev.*, 29(7), 989–1004.

Leduc, G., Vidal, L., Cartapanis, O., and Bard, E. (2009), Modes of eastern equatorial Pacific thermocline variability: Implications for ENSO dynamics over the last glacial period, *Paleoceanography*, 24, PA3202, doi:10.1029/2008PA001701.

Leduc, G., Vidal, L., Tachikawa, K., Rostek, F., Sonzogni, C., Beaufort, L., & Bard, E. (2007). Moisture transport across Central America as a positive feedback on abrupt climatic changes. *Nature*, 445(7130), 908–911. https://doi.org/10.1038/nature05578.

Lenton, Andrew & Mcinnes, Kathleen & O'Grady, Julian. (2015). Marine Projections of Warming and Ocean Acidification in the Australasian Region. *Australian Meteorological and Oceanographic Journal*. 65. S1-S28. 10.22499/2.6501.012.

Lewis, E., & Wallace, D. W. R. (1998). CO2SYS - Program developed for the CO2 system calculations. *ORNL/CDIAC-105 (Ed Center CDIA)*. https://doi.org/4735.

Lowenstein, T., & Hönisch, B. (2012). The Use of Mg/Ca as a Seawater Temperature Proxy. *The Paleontological Society Papers*, 18, 85-100. doi:10.1017/S1089332600002564.

Mekik, F., François, R., & Soon, M. (2007). A novel approach to dissolution correction of Mg/Ca-based paleothermometry in the tropical Pacific. *Paleoceanography*, 22, PA3217. https://doi.org/10.1029/2007PA001504.

Mann, M. E., R. S. Bradley, and M. K. Hughes (1998), Global-scale temperature patterns and climate forcing over the past six centuries, *Nature*, 392(6678), 779–787.

MARGO Project Members. (2009). Constraints on the magnitude and patterns of ocean cooling at the Last Glacial Maximum. *Nature Geosci* 2, 127–132. https://doi.org/10.1038/ngeo411.

Martínez, I., L. Keigwin, T. T. Barrows, Y. Yokoyama, and J. Southon (2003), La Niña-like conditions in the eastern equatorial Pacific and a stronger Choco jet in the northern Andes during the last glaciation, *Paleoceanography*, 18(2), 1033, doi:10.1029/2002PA000877.

Monteagudo, M.M., J. Lynch-Stieglitz, T.M. Marchitto and M.W. Schmidt (2021). Central Equatorial Pacific cooling during the Last Glacial Maximum. *Geophysical Research Letters*, 48, https://doi.org/10.1029/2020GL088592.

Otto-Bliesner, B. L., Schneider, R., Brady, E. C., Kucera, M., Abe-Ouchi, A., Bard, E., et al. (2009). A comparison of PMIP2 model simulations and the MARGO proxy reconstruction for tropical sea surface temperatures at last glacial maximum. *Climate Dynamics*, 32(6), 799–815. https://doi.org/10.1007/s00382-008-0509-0.

Rasmusson, E.M. and Carpenter, T.H. (1982) Variations in Tropical Sea Surface Temperature and Wind Associated with the Southern Oscillation/El Niño. *Monthly Weather Review*, 110, 354-384. https://doi.org/10.1175/1520-0493(1982)110<0354:VITSST>2.0.CO;2

Ravelo, Ana & Hillaire-Marcel, Claude. (2007). Chapter Eighteen The Use of Oxygen and Carbon Isotopes of Foraminifera in Paleoceanography. *Developments in Marine Geology.* 1. 10.1016/S1572-5480(07)01023-8.

Rippert, N. , Nürnberg, D. , Raddatz, J. , Maier, E. , Hathorne, E. C. , Bijma, J. and Tiedemann, R. (2016): Constraining foraminiferal calcification depths in the western Pacific warm pool, *Marine Micropaleontology*, 128, pp. 14-27. doi: 10.1016/j.marmicro.2016.08.004.

Rongstad, B. L., Marchitto, T. M., & Herguera, J. C. (2017). Understanding the effects of dissolution on the Mg/Ca paleothermometer in planktic foraminifera: Evidence from a novel individual foraminifera method. *Paleoceanography*, 193, 1–17. https://doi.org/10.1016/j.epsl.2007.03.025.

Rosell A., Grimalt J., Eglinton G. (1994) Organic Compounds as Proxy-Indicators of Sea Surface Palaeotemperature: The Uk37 Index. In: Duplessy JC., Spyridakis MT. (eds) Long-Term Climatic Variations. *NATO ASI Series (Series I: Global Environmental Change)*, vol 22. Springer, Berlin, Heidelberg. https://doi.org/10.1007/978-3-642-79066-9_9.

Sadekov, A. Y., Ganeshram, R., Pichevin, L., Berdin, R., McClymont, E., Elderfield, H., & Tudhope, A. W. (2013). Palaeoclimate reconstructions reveal a strong link between El niño-southern oscillation and tropical pacific mean state. *Nature Communications*, 4, [2692]. https://doi.org/10.1038/ncomms3692.

Schneider, B., G. Leduc, and W. Park (2010), Disentangling seasonal signals in holocene climate trends by satellite-model-proxy integration, *Paleoceanography*, 25, PA4217, doi:10.1029/2009PA001893.

Smith, T. M., Reynolds, R. W., Peterson, T. C., & Lawrimore, J. (2008). Improvements to NOAA's historical merged land–ocean surface temperature analysis (1880–2006). *Journal of Climate*, 21, 2283–2296.

Solomon, S., Q. Dahe, and M. Manning (2007), Technical summary, in Climate Change 2007, Contribution of Working Group I to the Fourth Assessment Report of the Intergovernmental Panel on Climate Change, pp. 19–91, Cambridge Univ. Press, Cambridge, U. K., and New York.

Tierney, J. E., Zhu, J., King, J., Malevich, S. B., Hakim, G. J., & Poulsen, C. J. (2020). Glacial cooling and climate sensitivity revisited. *Nature*, 584(7822), 569–573. https://doi.org/10.1038/s41586-020-2617-x.

Timmermann, A., J. Sachs, and O. E. Timm (2014), Assessing divergent SST behavior during the last 21 ka derived from alkenones and G. ruber-Mg/Ca in the equatorial Pacific, *Paleoceanography*, 29, 680–696, doi:10.1002/2013PA002598.

Qin, W., Carlson, L. T., Armbrust, E. V., Devol, A. H., Moffett, J. W., Stahl, D. A., & Ingalls, A. E. (2015). Confounding effects of oxygen and temperature on the TEX86 signature of

marine Thaumarchaeota. *Proceedings of the National Academy of Sciences of the United States of America*, 112(35), 10979–10984. https://doi.org/10.1073/pnas.1501568112.

Wycech, J.B. & Gill, E. & Rajagopalan, Balaji & Marchitto, T.M. & Molnar, P.H.. (2019). Multiproxy Reduced-Dimension Reconstruction of Pliocene Equatorial Pacific Sea Surface Temperatures. *Paleoceanography and Paleoclimatology*. 35. 10.1029/2019PA003685.

Wycech, J. B., Kelly, D. C., Kitajima, K., Kozdon, R., Orland, I. J., & Valley, J. W. (2018). Combined effects of gametogenic calcification and dissolution on δ18O measurements of the planktic foraminifer Trilobatus sacculifer. *Geochemistry Geophysics Geosystems*, 18, 1–15. https://doi.org/10.1029/2018GC007908.

Xu, J., Kuhnt, W., Holbourn, A., Regenberg, M., & Andersen, N. (2010). Indo-pacific warm pool variability during the Holocene and last glacial maximum. *Paleoceanography*, 25(4), PA4230. https://doi.org/10.1029/2010PA001934.

Zachos, J., Pagani, M., Sloan, L., Thomas, E., & Billups, K. (2001). Trends, rhythms, and aberrations in global climate 65 ma to present. *Science*, 292(5517), 686–693. https://doi.org/10.1126/science.1059412.

Zhu, J., et al. (2017), Reduced ENSO variability at the LGM revealed by an isotope-enabled Earth system model, *Geophys. Res. Lett.*, 44, 6984–6992, doi:10.1002/2017GL073406.

APPENDIX

Figure A1. Bayesian calibration vs Dekens calibration for Tierney LGM data

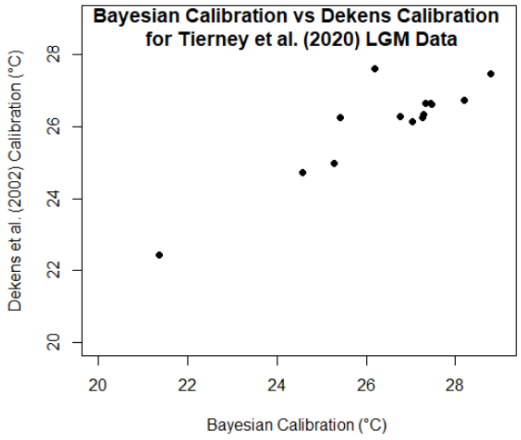

Text (Figure A1). We compared the originally calibrated Tierney et al. (2020) data against the Dekens et al. (2002) calibration used for the other dataset to see if there were significant differences between the two groups. We performed a t-test and found a p-value of 0.07565. Since this is > 0.05, we fail to reject the null hypothesis. This means that the samples did not provide sufficient evidence to conclude that the true difference in means is equal to 0. If our p value were less than our alpha value of 0.05, we would be able to reject the null and say the true difference in means is not equal to 0 (statistically significant).

Table A1. Core data used in this study

Core	Lat (°N)	Long (°E)	Depth (km)	LH Mg/Ca & Uk37	LH or Modern Temp	LGM Mg/Ca & Uk37	LGM Temp	$\Delta[CO_3^{2-}]$	Proxy	SST change	Reference
GIK18500-3	-14.98	120.70	1.167	5.20	30.5	4.00	27.5	18.5	mg	-2.9	Xu et al., (2010)
GIK18507-3	-13.85	120.00	2.450	4.32	28.8	3.42	26.2	9.1	mg	-2.6	Xu et al., (2010)
MD01-2378	-13.08	121.79	1.783	4.63	30.0	3.67	27.4	-0.7	mg	-2.6	Xu et al., (2008)
GIK18473-2	-11.52	122.42	2.468	4.67	29.7	4.27	28.7	8.1	mg	-1.0	Xu et al., (2010)
GIK18475-3	-11.03	121.70	1.774	4.35	28.7	3.66	26.8	13.7	mg	-1.9	Xu et al., (2010)
SO18480-3	-12.06	121.65	2.299	4.46	29.1	3.47	26.3	10.3	mg	-2.8	Dang et al., (2020)
MD98-2165	-9.65	118.40	2.100	4.49	27.9	3.47	25.1	11.9	mg	-2.9	Levi et al., (2007)
GeoB10069-3	-9.01	120.02	1.250	4.01	27.6	3.49	26.1	17.2	mg	-1.5	Gibbons et al., (2014)

GIK18476-2	-10.95	120.99	0.986	NA	28.3	3.59	26.3	20.3	mg	-2.1	Xu et al., (2010)
GIK18477-4	-10.83	120.67	1.478	4.38	28.7	3.69	26.8	15.3	mg	-1.9	Xu et al., (2010)
MD98-2170	-10.59	125.39	0.832	5.35	30.5	4.14	27.7	24.0	mg	-2.8	Stott et al., (2007)
GIK18462-3	-9.09	129.24	1.421	4.48	29.0	3.59	26.6	13.3	mg	-2.5	Xu et al., (2010)
GeoB10042-1	-7.11	104.64	2.454	NA	28.3	3.45	25.0	11.5	mg	-3.3	Setiawan et al., (2015)
GeoB10043-3	-7.31	105.06	2.171	4.32	27.4	3.53	25.2	13.6	mg	-2.2	Setiawan et al., (2015)
GIK18459-3	-8.50	128.17	1.744	4.59	29.4	3.64	26.8	11.0	mg	-2.6	Xu et al., (2010)
GIK18460-3	-8.79	128.64	1.875	4.67	29.6	3.35	25.9	9.8	mg	-3.7	Xu et al., (2010)
VM28-234	-7.10	159.00	2.719	4.38	29.3	3.26	26.0	0.8	mg	-3.3	Monteagudo et al., (2021)
GeoB10038-4	-5.94	103.25	1.819	4.33	27.4	3.61	25.4	15.6	mg	-2.0	Mohtadi et al., (2010)
SO139-74KL	-6.54	103.83	1.690	4.40	28.7	3.16	25.0	16.6	mg	-3.7	Wang et al., (2018)
MD98-2161	-5.21	117.48	1.185	4.64	29.0	3.59	26.1	23.2	mg	-2.9	Fan et al., (2018)
SO217-18540	-6.87	119.58	1.189	4.50	28.6	3.48	25.8	23.4	mg	-2.9	Schröder et al., (2018)
MD98-2176	-5.00	133.44	2.382	5.08	30.6	3.99	28.0	7.8	mg	-2.7	Stott et al., (2007)
MD98-2162	-4.69	117.90	1.855	5.11	29.1	3.75	25.7	17.8	mg	-3.4	Visser et al., (2003)
SO217-18515	-3.63	119.36	0.688	4.77	28.9	3.59	25.7	33.8	mg	-3.2	Schröder et al., (2016)
V21-30	-1.22	-89.68	0.617	3.12	25.3	2.61	23.4	5.0	mg	-2.0	Koutavas and Joanides, (2012)
GeoB10029-4	-1.49	100.13	0.964	5.07	29.0	3.87	26.0	18.5	mg	-3.0	Mohtadi et al., (2010)
TGS931	-2.41	122.62	1.912	NA	29.0	3.62	26.5	16.7	mg	-2.5	Schröder et al., (2018)

GeoB17426-3	-2.19	150.86	1.367	5.14	29.2	4.06	26.6	16.9	mg	-2.6	Hollstein et al., (2018)
KX973-21-2	-1.42	157.98	1.897	NA	29.4	3.73	27.1	11.0	mg	-2.3	Dang et al., (2020)
ML1208-13BB	-0.22	-155.96	3.050	NA	27.2	3.03	25.3	-0.8	mg	-1.9	Monteagudo et al., (2021)
ML1208-15GC	0.16	-156.12	3.597	NA	27.2	2.72	24.2	-5.0	mg	-2.9	Monteagudo et al., (2021)
ML1208-18GC	0.59	-156.66	3.362	NA	27.2	3.09	25.6	-3.2	mg	-1.6	Monteagudo et al., (2021)
ML1208-19GC	0.83	-156.87	2.956	3.43	26.6	2.90	24.7	-0.1	mg	-1.9	Monteagudo et al., (2021)
TR163-20B	0.79	-93.84	3.200	NA	24.5	1.97	20.7	-6.1	mg	-3.8	Lea et al., (2000)
TR163-22	0.52	-92.40	2.830	2.48	23.1	2.12	21.4	-3.0	mg	-1.7	Lea et al., (2006)
MV1014-17JC/09MC	-0.18	-85.87	2.868	2.46	23.0	2.31	22.3	-3.0	mg	-0.7	Hertzberg et al., (2016)
SO217-18519	-0.57	118.11	1.658	4.67	29.3	3.58	26.3	18.2	mg	-3.0	Schröder et al., (2018)
MD10-3340	-0.52	128.72	1.094	4.66	29.4	3.59	26.5	14.6	mg	-2.9	Dang et al., (2020)
ODP-806B	0.32	159.36	2.520	NA	29.3	3.13	25.4	3.6	mg	-3.8	Lea et al., (2000)
ML1208-27BB	2.77	-159.29	3.331	NA	27.5	3.23	26.2	-7.3	mg	-1.2	Monteagudo et al., (2021)
ML1208-28BB	2.97	-159.20	3.153	NA	27.5	3.05	25.5	-5.1	mg	-2.0	Monteagudo et al., (2021)
ML1208-20BB/21MC	1.27	-157.26	2.850	3.58	27.1	2.97	25.0	-0.3	mg	-2.1	Monteagudo et al., (2021)

TR163-18	2.81	-89.85	2.030	NA	26.0	2.39	22.6	0.7	mg	-3.4	Lea et al., (2000)
TR163-19	2.26	-90.95	2.348	2.99	25.1	2.40	22.7	-0.8	mg	-2.4	Lea et al., (2000)
SO217-18522	1.40	119.08	0.975	4.68	29.4	3.75	26.9	16.4	mg	-2.5	Schröder et al., (2018)
MD97-2140	2.02	141.46	2.547	NA	29.3	3.70	26.0	7.8	mg	-3.3	de Garidel-Thoron et al., (2005)
MD97-2138	1.25	146.14	1.960	4.60	27.9	3.51	24.9	18.3	mg	-3.0	de Garidel-Thoron et al., (2007)
ML1208-31BB	4.68	-160.05	2.857	NA	27.9	3.29	26.2	-1.0	mg	-1.7	Monteagudo et al., (2021)
MD98-2178	3.62	118.70	1.194	4.49	29.1	3.48	26.3	12.0	mg	-2.8	Fan et al., (2018)
SO217-18526	3.61	118.17	1.524	4.72	29.4	3.60	26.4	18.2	mg	-3.0	Schröder et al., (2018)
ML1208-06GC	6.41	-161.01	2.371	NA	28.2	3.16	25.5	5.8	mg	-2.7	Monteagudo et al., (2021)
ML1208-36BB	6.83	-161.04	2.855	NA	28.2	3.37	26.4	-0.6	mg	-1.8	Monteagudo et al., (2021)
ML1208-32BB	5.20	-160.43	2.926	NA	28.1	3.23	26.0	-1.9	mg	-2.1	Monteagudo et al., (2021)
MV1014-08JC/07MC	6.23	-86.04	1.993	3.32	26.2	2.88	24.6	0.7	mg	-1.6	Hertzberg et al., (2016)
MD01-2390	6.64	113.41	1.545	4.61	28.4	3.76	26.1	7.5	mg	-2.3	Steinke et al., (2006)
MD06-3067	6.51	126.50	1.575	NA	28.8	3.78	27.4	7.6	mg	-1.4	Bolliet et al., (2011)
MD98-2181	6.30	125.83	2.114	5.19	30.8	3.96	27.8	9.3	mg	-3.0	Stott et al., (2002)

ML1208-37BB	7.04	-161.63	2.798	NA	28.1	3.24	26.0	-0.6	mg	-2.1	Monteagudo et al., (2021)
MD02-2529	8.21	-84.12	1.619	3.80	27.7	3.03	25.1	2.1	mg	-2.5	Leduc et al., (2007)
ME005A-43JC	7.86	-83.61	1.368	4.12	27.3	3.33	25.0	2.9	mg	-2.4	Benway et al., (2006)
ODP-1242	7.86	-83.61	1.364	4.33	29.1	3.32	26.1	2.9	mg	-3.0	Lea et al., (2000)
MD97-2141	8.47	121.17	3.633	NA	28.8	3.51	25.7	0.4	mg	-3.1	Rosenthal et al., (2003)
3cBX	8.02	139.64	2.829	4.23	27.7	3.26	24.8	1.7	mg	-2.9	Sagawa et al., (2012)
GIK17957-2	10.90	115.31	2.195	4.13	28.5	3.98	28.0	5.4	mg	-0.4	Xu et al., (2010)
GIK17954-3	14.80	111.53	1.515	4.09	28.2	3.07	25.0	8.5	mg	-3.2	Xu et al., (2010)
GIK18506-2	-15.31	119.50	2.410	4.52	30.5	3.44	27.3	9.4	mg	-3.3	Xu et al., (2010)
so189-039kl	-0.79	99.91	0.517	5.33	29.8	3.98	26.2	34.4	mg	-3.6	Mohtadi et al., (2014)
Fr10-95 GC5	-14.01	121.03	2.472	NA	28.4	0.919	26.6	NA	uk	-1.8	Lee et al., (2004)
ODP 846	-3.095	-90.82	3.307	0.803	22.3	0.739	20.3	NA	uk	-2.0	Lawrence et al., (2006)
tr163-31	-3.62	-83.97	3.205	NA	22.8	0.746	20.6	NA	uk	-2.2	Dubois et al., (2009)
vm19-30	-3.38	-83.52	3.091	0.806	22.4	0.738	20.3	NA	uk	-2.1	Koutavas and Sachs (2008)
knr195-5-cdh26	-3.99	-81.31	1.023	0.794	22.0	0.728	20.0	NA	uk	-2.0	Bova et al., (2015)
vm21-30	-1.22	-89.68	0.617	0.880	24.9	0.841	23.5	NA	uk	-1.4	Koutavas and Sachs (2008)
rc11-238	-1.51	-85.82	2.573	NA	23.7	0.783	21.7	NA	uk	-2.0	Koutavas and Lynch-Stieglitz (2003)
vm19-28	-2.37	-84.65	2.720	0.847	23.8	0.770	21.3	NA	uk	-2.5	Koutavas and

											Joanides, (2012)
me0005a-27jc	-1.85	-82.79	2.203	0.864	24.4	0.811	22.6	NA	uk	-1.8	Dubois et al., (2009)
W8402A-14GC	0.95	-138.96	4.287	0.957	28.3	0.926	26.9	NA	uk	-1.4	Prahl et al., (1989)
ODP 847	0.193	-95.32	3.355	NA	24.6	0.753	20.8	NA	uk	-3.8	Lee et al., (2004)
tr163-22	0.52	-92.40	2.830	0.859	24.2	0.797	22.1	NA	uk	-2.1	Dubois et al., (2009)
me0005a-24jc/ME0005A-21MC4	0.02	-86.46	2.941	0.915	26.4	0.819	22.8	NA	uk	-3.6	Kienast et al., (2006)
ODP 1239A	-0.67	-82.08	1.415	NA	25.2	0.781	21.6	NA	uk	-3.5	Shaari et al., (2013)
vm19-27	-0.47	-82.07	1.373	0.917	26.5	0.871	24.6	NA	uk	-1.9	Koutavas and Lynch-Stieglitz (2003)
tr163-19	2.26	-90.95	2.348	NA	26.0	0.856	24.1	NA	uk	-1.9	Dubois et al., (2009)
KH92-1-5cBX	3.53	141.87	2.282	0.964	28.6	0.974	29.1	NA	uk	0.5	Ohkouchi et al., (1994)
gik17964-2	6.16	112.21	1.556	0.958	28.4	0.894	25.6	NA	uk	-2.8	Pelejero et al., (2010)
md01-2390	6.64	113.40	1.545	NA	28.8	0.922	26.7	NA	uk	-2.1	Steinke e al., (2008)
md06-3075	6.48	125.83	1.878	0.972	29.0	0.916	26.5	NA	uk	-2.6	Fraser et al., (2014)
md02-2529	8.21	-84.12	1.619	0.951	28.0	0.901	25.9	NA	uk	-2.2	Leduc et al., (2007)
me0005a-43jc	7.86	-83.61	1.368	0.96	28.5	0.909	26.1	NA	uk	-2.4	Benway et al., (2006)
md97-2151	8.73	109.87	1.598	0.946	27.8	0.889	25.3	NA	uk	-2.5	Yamamoto et al., (2013)
gik17961-2/GIK17961-1	8.51	112.33	1.795	0.956	28.3	0.891	25.4	NA	uk	-2.8	Pelejero et al., (2010)

GIK16969-1	9.06	-85.63	3.387	0.948	27.9	0.892	25.5	NA	uk	-2.4	Lee et al., (2004)
gik18252-3	9.25	109.39	1.273	NA	28.1	0.864	24.4	NA	uk	-3.7	Kienast et al., (2001)
ODP 1143	9.36	113.29	2.772	NA	28.6	0.916	26.4	NA	uk	-2.1	Li et al., (2011)

Text (Table A1).
LH and LGM temperatures from Monteagudo et al. (2021) were calculated using the Dekens et al. (2002) dissolution correction equation with +0.6°C adjustment (which prevents an overestimation of the magnitude of LGM cooling). For sites that did not have LH data, we used the contemporary ERSST data as estimates.

Proper estimates of the $\Delta[CO_3^{2-}]$ for the two Tierney LH Mg/Ca sites were calculated using the seafloor $\Delta[CO_3^{2-}]$ values from the nearest WOCE transects and the carbonate system calculator CO2Sys (version 2.1 for Excel) with default dissociation constants (Lewis and Wallace, 1998). We then calibrated these temperatures using the same Dekens et al. (2002) dissolution correction equation. Other temperatures are as reported by Tierney et al. (2020) using BAYSPLINE.

Table A2. Statistical overview from various reconstructions

Proxies Used in Reconstruction	Mean Anomaly (± standard deviation)	Highest Cooling Anomaly	Lowest Cooling Anomaly	Range in Cooling Anomalies
Both (Mg/Ca and $U^{K'}_{37}$)	-2.26°C ± 0.39°C	-3.72°C	-1.25°C	2.47°C
Mg/Ca	-2.25°C ± 0.41°C	-3.58°C	-1.24°C	2.34°C
$U^{K'}_{37}$	-1.57°C ± 0.36°C	-2.94°C	-0.81°C	2.13°C